Supplementary material for "On water waves generated by a bottom obstacle translating at a subcritical speed"

Peter H.-Y. Lo and Philip L.-F. Liu

This is the supplementary material for the paper entitled "On water waves generated by a bottom obstacle translating at a subcritical speed". This document shows the velocity solutions based on the linear and fully dispersive wave model, outlines the derivation process for the analytical solutions based on the linear and weakly dispersive wave model, provides descriptions on the numerical models used, and presents the numerical results from relevant validation tests.

S.1. Velocity solutions for the linear and fully dispersive wave model

The velocity solutions based on the linear and fully dispersive wave model for waves generated by a translating bottom obstacle can be calculated from (2.5) and (2.9) in the main paper as

$$\begin{cases} u(r,\theta,z,t) = u_{Fr}(r,\theta,z,t) + u_{+}(r,\theta,z,t) \\ u_{Fr} = -\dfrac{1}{2\pi}\displaystyle\int_0^{2\pi}\int_0^{\infty} \frac{q\widetilde{\overline{B_0}}(q,\psi)}{\cosh(\mu q)}\cos\psi\Big[\frac{1}{Fr\cos\psi}\cosh(\mu q z) + \mu q\cdot Fr\cos\psi\sinh(\mu q z)\Big] \\ \qquad\qquad \dfrac{Fr^2\cos^2\psi}{D^2 - Fr^2\cos^2\psi} e^{-iq\cdot Fr\cos\psi\cdot t} e^{iqr\cos(\psi-\theta)} dq d\psi \\ u_{+} = \dfrac{1}{2\pi}\displaystyle\int_0^{2\pi}\int_0^{\infty} \frac{q\widetilde{\overline{B_0}}(q,\psi)}{\cosh(\mu q)}\cos\psi\Big[\frac{1}{D}\cosh(\mu q z) + \mu q D\sinh(\mu q z)\Big] \\ \qquad \Big(\dfrac{Fr\cos\psi}{2(D - Fr\cos\psi)} e^{-iqDt} + \dfrac{Fr\cos\psi}{2(D + Fr\cos\psi)} e^{iqDt}\Big) e^{iqr\cos(\psi-\theta)} dq d\psi \end{cases} \tag{S.1.1}$$

$$\begin{cases} v(r,\theta,z,t) = v_{Fr}(r,\theta,z,t) + v_{+}(r,\theta,z,t) \\ v_{Fr} = -\dfrac{1}{2\pi}\displaystyle\int_0^{2\pi}\int_0^{\infty} \frac{q\widetilde{\overline{B_0}}(q,\psi)}{\cosh(\mu q)}\sin\psi\Big[\frac{1}{Fr\cos\psi}\cosh(\mu q z) + \mu q\cdot Fr\cos\psi\sinh(\mu q z)\Big] \\ \qquad\qquad \dfrac{Fr^2\cos^2\psi}{D^2 - Fr^2\cos^2\psi} e^{-iq\cdot Fr\cos\psi\cdot t} e^{iqr\cos(\psi-\theta)} dq d\psi \\ v_{+} = \dfrac{1}{2\pi}\displaystyle\int_0^{2\pi}\int_0^{\infty} \frac{q\widetilde{\overline{B_0}}(q,\psi)}{\cosh(\mu q)}\sin\psi\Big[\frac{1}{D}\cosh(\mu q z) + \mu q D\sinh(\mu q z)\Big] \\ \qquad \Big(\dfrac{Fr\cos\psi}{2(D - Fr\cos\psi)} e^{-iqDt} + \dfrac{Fr\cos\psi}{2(D + Fr\cos\psi)} e^{iqDt}\Big) e^{iqr\cos(\psi-\theta)} dq d\psi \end{cases} \tag{S.1.2}$$

and

$$\begin{cases} w(r,\theta,z,t) = w_{_{Fr}}(r,\theta,z,t) + w_{+}(r,\theta,z,t) \\ w_{_{Fr}} = \dfrac{i\mu}{2\pi}\displaystyle\int_0^{2\pi}\int_0^{\infty} \dfrac{q\widetilde{\widetilde{B_0}}(q,\psi)}{\cosh(\mu q)}\Big[\dfrac{1}{Fr\cos\psi}\sinh(\mu q z) + \mu q\cdot Fr\cos\psi\cosh(\mu q z)\Big] \\ \qquad\qquad \dfrac{Fr^2\cos^2\psi}{D^2 - Fr^2\cos^2\psi} e^{-iq\cdot Fr\cos\psi\cdot t} e^{iqr\cos(\psi-\theta)} dq d\psi \\ w_{+} = -\dfrac{i\mu}{2\pi}\displaystyle\int_0^{2\pi}\int_0^{\infty} \dfrac{q\widetilde{\widetilde{B_0}}(q,\psi)}{\cosh(\mu q)}\Big[\dfrac{1}{D}\sinh(\mu q z) + \mu q D\cosh(\mu q z)\Big] \\ \qquad \Big(\dfrac{Fr\cos\psi}{2(D - Fr\cos\psi)} e^{-iqDt} + \dfrac{Fr\cos\psi}{2(D + Fr\cos\psi)} e^{iqDt}\Big) e^{iqr\cos(\psi-\theta)} dq d\psi \end{cases}, \tag{S.1.3}$$

which are normalised by $\epsilon\sqrt{gd}$. The expressions for the velocities are highly similar to those for the free surface elevation, (2.18) in the main paper, but with the addition of the terms in the square brackets and the $\cos\psi$ or $\sin\psi$, if any, in front of the brackets. Again, $u_{_{Fr}}$, $v_{_{Fr}}$, and $w_{_{Fr}}$ are the trapped wave solutions – they move with the bottom obstacle and do not change shape.

Similarly to the free surface solutions, for large r and $0 < Fr < 1$, the far-field solutions for the velocities can be derived:

$$\begin{aligned} u_{\text{far}} \;=\; & \frac{1}{\sqrt{2\pi}} r^{-\frac{1}{2}} \int_0^{\infty} \frac{\widetilde{\widetilde{B_0}}(q,\theta)}{\cosh(\mu q)} \frac{Fr\cos\theta}{2(D - Fr\cos\theta)} q^{\frac{1}{2}} \\ & \cos\theta\Big[\frac{1}{D}\cosh(\mu q z) + \mu q D\sinh(\mu q z)\Big] e^{i\left(q(r-Dt)-\frac{\pi}{4}\right)} dq \\ & + \frac{1}{\sqrt{2\pi}} r^{-\frac{1}{2}} \int_0^{\infty} \frac{\widetilde{\widetilde{B_0}}(q,\pi+\theta)}{\cosh(\mu q)} \frac{Fr\cos\theta}{2(D - Fr\cos\theta)} q^{\frac{1}{2}} \\ & \cos\theta\Big[\frac{1}{D}\cosh(\mu q z) + \mu q D\sinh(\mu q z)\Big] e^{-i\left(q(r-Dt)-\frac{\pi}{4}\right)} dq \end{aligned}, \tag{S.1.4}$$

$$\begin{aligned} v_{\text{far}} \;=\; & \frac{1}{\sqrt{2\pi}} r^{-\frac{1}{2}} \int_0^{\infty} \frac{\widetilde{\widetilde{B_0}}(q,\theta)}{\cosh(\mu q)} \frac{Fr\cos\theta}{2(D - Fr\cos\theta)} q^{\frac{1}{2}} \\ & \sin\theta\Big[\frac{1}{D}\cosh(\mu q z) + \mu q D\sinh(\mu q z)\Big] e^{i\left(q(r-Dt)-\frac{\pi}{4}\right)} dq \\ & + \frac{1}{\sqrt{2\pi}} r^{-\frac{1}{2}} \int_0^{\infty} \frac{\widetilde{\widetilde{B_0}}(q,\pi+\theta)}{\cosh(\mu q)} \frac{Fr\cos\theta}{2(D - Fr\cos\theta)} q^{\frac{1}{2}} \\ & \sin\theta\Big[\frac{1}{D}\cosh(\mu q z) + \mu q D\sinh(\mu q z)\Big] e^{-i\left(q(r-Dt)-\frac{\pi}{4}\right)} dq \end{aligned}, \tag{S.1.5}$$

and

$$\begin{aligned} w_{\text{far}} \;=\; & -\frac{i\mu}{\sqrt{2\pi}} r^{-\frac{1}{2}} \int_0^{\infty} \frac{\widetilde{\widetilde{B_0}}(q,\theta)}{\cosh(\mu q)} \frac{Fr\cos\theta}{2(D - Fr\cos\theta)} q^{\frac{1}{2}} \\ & \Big[\frac{1}{D}\sinh(\mu q z) + \mu q D\cosh(\mu q z)\Big] e^{i\left(q(r-Dt)-\frac{\pi}{4}\right)} dq \\ & - \frac{i\mu}{\sqrt{2\pi}} r^{-\frac{1}{2}} \int_0^{\infty} \frac{\widetilde{\widetilde{B_0}}(q,\pi+\theta)}{\cosh(\mu q)} \frac{Fr\cos\theta}{2(D - Fr\cos\theta)} q^{\frac{1}{2}} \\ & \Big[\frac{1}{D}\sinh(\mu q z) + \mu q D\cosh(\mu q z)\Big] e^{-i\left(q(r-Dt)-\frac{\pi}{4}\right)} dq \end{aligned}. \tag{S.1.6}$$

The horizontal velocities in the x and y directions can be converted to velocities in the r and θ

directions by

$$\begin{array}{l} R(r,\theta,z,t) = u(r,\theta,z,t)\cos\theta + v(r,\theta,z,t)\sin\theta \\ \Theta(r,\theta,z,t) = -u(r,\theta,z,t)\sin\theta + v(r,\theta,z,t)\cos\theta \end{array} . \tag{S.1.7}$$

From (S.1.4) and (S.1.5), the far-field velocity solutions in the r and θ directions then become

$$\begin{aligned} R_{\text{far}} \quad = \quad & \frac{1}{\sqrt{2\pi}} r^{-\frac{1}{2}} \int_0^\infty \frac{\widetilde{\widetilde{B_0}}(q,\theta)}{\cosh(\mu q)} \frac{Fr\cos\theta}{2(D - Fr\cos\theta)} q^{\frac{1}{2}} \\ & \left[\frac{1}{D}\cosh(\mu q z) + \mu q D \sinh(\mu q z)\right] e^{i\left(q(r-Dt)-\frac{\pi}{4}\right)} dq \\ & + \frac{1}{\sqrt{2\pi}} r^{-\frac{1}{2}} \int_0^\infty \frac{\widetilde{\widetilde{B_0}}(q,\pi+\theta)}{\cosh(\mu q)} \frac{Fr\cos\theta}{2(D - Fr\cos\theta)} q^{\frac{1}{2}} \\ & \left[\frac{1}{D}\cosh(\mu q z) + \mu q D \sinh(\mu q z)\right] e^{-i\left(q(r-Dt)-\frac{\pi}{4}\right)} dq \end{aligned} , \tag{S.1.8}$$

and

$$\Theta_{\text{far}} = 0. \tag{S.1.9}$$

The results suggest that in the far field, the waves spread strictly radially, as the velocity in the θ direction is zero.

The method used in Section 2.3 in the main paper to obtain the far-field leading wave solution (valid for large r and near $r = t$) for the surface elevation can be repeated to obtain the velocity solutions for the far-field leading wave. The derivation process is essentially identical – the terms in the square brackets in (S.1.4), (S.1.5), and (S.1.6) simplify to either one or zero as $q \to 0$. The only new terms in the velocity solutions are $\cos\theta$ in (S.1.4) and $\sin\theta$ in (S.1.5). The final results are

$$u_{\text{lead}}(r,\theta,t) = \eta_{\text{lead}}(r,\theta,t)\cos\theta, \quad v_{\text{lead}}(r,\theta,t) = \eta_{\text{lead}}(r,\theta,t)\sin\theta, \quad w_{\text{lead}}(r,\theta,t) = 0, \tag{S.1.10}$$

or

$$R_{\text{lead}}(r,\theta,t) = \eta_{\text{lead}}(r,\theta,t), \quad \Theta_{\text{lead}}(r,\theta,t) = 0, \quad w_{\text{lead}}(r,\theta,t) = 0, \tag{S.1.11}$$

where the expression for η_{lead} has been given in (2.22) in the main paper.

Since the longest wave, corresponding to $q = 0$, travels the fastest to become the leading wave, the far-field leading waves are long waves. Consistent with the characteristics of long waves, the above velocity solutions for the far-field leading wave show no depth variation in the horizontal velocities and no vertical velocity ($w_{\text{lead}} = 0$).

S.2. Analytical solutions for the linear and weakly dispersive wave model

The derivation of the analytical solutions for LWD in constant water depth is essentially the same as that for the linear and fully dispersive wave model presented in Section 2.1 in the main paper. The dimensionless continuity equation reads

$$\eta_t + u_{\alpha,x} + v_{\alpha,y} + \alpha_{11}(u_{\alpha,xxx} + u_{\alpha,xyy} + v_{\alpha,yyy} + v_{\alpha,xxy}) = B_t + \alpha_{12}(B_{txx} + B_{tyy}), \tag{S.2.1}$$

and the momentum equations read

$$u_{\alpha,t} + \alpha_{21}(u_{\alpha,xxt} + v_{\alpha,xyt}) + \eta_x = \alpha_{22} B_{xtt}, \quad v_{\alpha,t} + \alpha_{21}(u_{\alpha,xyt} + v_{\alpha,yyt}) + \eta_y = \alpha_{22} B_{ytt}, \tag{S.2.2}$$

where α_{11}, α_{12}, α_{21}, and α_{22} are constants of order $O(\mu^2)$:

$$\alpha_{11} = \mu^2\left(\frac{1}{2}\alpha^2 + \alpha + \frac{1}{3}\right), \quad \alpha_{12} = \mu^2\left(\alpha + \frac{1}{2}\right), \quad \alpha_{21} = \mu^2\left(\frac{1}{2}\alpha^2 + \alpha\right), \quad \alpha_{22} = \mu^2\alpha, \tag{S.2.3}$$

where an optimal value $\alpha = -0.531$ was suggested by Nwogu (1993). We recall that LWD has a formal accuracy of $O(\mu^2)$, and that the velocity solutions, $u_\alpha(x, y, t)$ and $v_\alpha(x, y, t)$, are solved for at a characteristic depth $z = z_\alpha = \alpha$. The velocity profiles can be recovered as

$$\begin{cases} U(x,y,z,t) = u_\alpha - \mu^2(\frac{1}{2}z^2 + z - \frac{1}{2}\alpha^2 - \alpha)(u_{\alpha,xx} + v_{\alpha,xy}) + \mu^2(z-\alpha)B_{xt} + O(\mu^4) \\ V(x,y,z,t) = v_\alpha - \mu^2(\frac{1}{2}z^2 + z - \frac{1}{2}\alpha^2 - \alpha)(u_{\alpha,xy} + v_{\alpha,yy}) + \mu^2(z-\alpha)B_{yt} + O(\mu^4) \end{cases}. \tag{S.2.4}$$

The initial conditions to be imposed are

$$\eta(x,y,t=0) = 0, \quad U(x,y,z=0,t=0) = 0, \quad V(x,y,z=0,t=0) = 0, \tag{S.2.5}$$

i.e., the free surface is initially quiescent, and the flow velocities on the free surface are zero initially. The velocity conditions translate to

$$\begin{cases} U(x,y,0,0) = u_\alpha(t=0) + \alpha_{21}\Big(u_{\alpha,xx}(t=0) + v_{\alpha,xy}(t=0)\Big) - \alpha_{22}B_{xt} + O(\mu^4) \\ V(x,y,0,0) = v_\alpha(t=0) + \alpha_{21}\Big(u_{\alpha,xy}(t=0) + v_{\alpha,yy}(t=0)\Big) - \alpha_{22}B_{yt} + O(\mu^4) \end{cases}. \tag{S.2.6}$$

According to (S.2.4),

$$\begin{cases} u_\alpha(x,y,0) = U(x,y,0,0) + O(\mu^2) = 0 + O(\mu^2) \\ v_\alpha(x,y,0) = V(x,y,0,0) + O(\mu^2) = 0 + O(\mu^2) \end{cases}, \tag{S.2.7}$$

i.e., to the leading order, $O(1)$, u_α and $U(x, y, 0, 0)$, as well as v_α and $V(x, y, 0, 0)$, are interchangeable. Therefore, without affecting the formal accuracy of LWD, which is accurate to $O(\mu^2)$, the terms multiplied by α_{21} in (S.2.6) can be replaced with zero, since $U(x, y, z = 0, t = 0)$ and $V(x, y, z = 0, t = 0)$ and their spatial derivatives are zero. The initial conditions to be imposed then become

$$\eta(x,y,0) = 0, \quad u_\alpha(x,y,0) = \alpha_{22}B_{xt}, \quad v_\alpha(x,y,0) = \alpha_{22}B_{yt}. \tag{S.2.8}$$

Applying the double Fourier transforms in space and the Laplace transform in time to (S.2.1) and (S.2.2), and imposing the initial conditions (S.2.8), we write the transformed governing equations as

$$\begin{cases} s\overline{\overline{\eta}} + ik(1-\alpha_{11}q^2)\overline{\overline{u_\alpha}} + il(1-\alpha_{11}q^2)\overline{\overline{v_\alpha}} = (1-\alpha_{12}q^2)(s\overline{\overline{B}} - \overline{\widetilde{B_0}}) \\ \overline{\overline{u_\alpha}}(s - sk^2\alpha_{21}) = ik\alpha_{22}(s^2\overline{\overline{B}} - s\overline{\widetilde{B_0}}) - ik\overline{\overline{\eta}} + skl\alpha_{21}\overline{\overline{v_\alpha}} + O(\mu^4) \\ \overline{\overline{v_\alpha}}(s - sl^2\alpha_{21}) = il\alpha_{22}(s^2\overline{\overline{B}} - s\overline{\widetilde{B_0}}) - il\overline{\overline{\eta}} + skl\alpha_{21}\overline{\overline{u_\alpha}} + O(\mu^4) \end{cases}, \tag{S.2.9}$$

where $q^2 = k^2 + l^2$ is again used to simplify the notations. The latter two equations can be combined to express $\overline{\overline{u_\alpha}}$ and $\overline{\overline{v_\alpha}}$ in terms of $\overline{\overline{\eta}}$:

$$\overline{\overline{u_\alpha}} = \frac{1}{s}\frac{ik}{1-\alpha_{21}q^2}\Big(\alpha_{22}(s^2\overline{\overline{B}} - s\overline{\widetilde{B_0}}) - \overline{\overline{\eta}}\Big), \quad \overline{\overline{v_\alpha}} = \frac{1}{s}\frac{il}{1-\alpha_{21}q^2}\Big(\alpha_{22}(s^2\overline{\overline{B}} - s\overline{\widetilde{B_0}}) - \overline{\overline{\eta}}\Big). \tag{S.2.10}$$

Substituting the above expressions back into the first equation in (S.2.9) allows $\overline{\overline{\eta}}$ to be solved for as

$$\overline{\overline{\eta}} = \frac{1}{s^2 + D^2q^2}(s^2\overline{\overline{B}} - s\overline{\widetilde{B_0}})(1 - \alpha_{12}q^2 + \alpha_{22}D^2q^2), \tag{S.2.11}$$

where

$$D(q) = \sqrt{\frac{1-\alpha_{11}q^2}{1-\alpha_{21}q^2}} \tag{S.2.12}$$

is the normalised wave speed of LWD in 2DH.

For a bottom obstacle translating at a normalised constant speed Fr in the x direction, the transformed free surface solution simplifies to

$$\tilde{\tilde{\tilde{\eta}}} = \frac{s}{s+ikFr}\frac{1}{s^2+D^2q^2}(-ikFr\widetilde{\widetilde{B_0}})(1-\alpha_{12}q^2+\alpha_{22}D^2q^2), \tag{S.2.13}$$

for which an inverse Laplace transform is available. After simplification and converting to polar coordinates, the solution for the free surface is

$$\begin{cases} \eta(r,\theta,t) = \eta_{Fr}(r,\theta,t) + \eta_{+}(r,\theta,t) \\ \eta_{Fr}(r,\theta,t) = -\dfrac{1}{2\pi}\displaystyle\int_0^{2\pi}\int_0^{\infty} q(1-\alpha_{12}q^2+\alpha_{22}D^2q^2)\widetilde{\widetilde{B_0}}\frac{Fr^2\cos^2\psi}{D^2-Fr^2\cos^2\psi} \\ \qquad\qquad e^{-iqFr\cos\psi t}e^{iqr\cos(\psi-\theta)}dqd\psi \\ \eta_{+}(r,\theta,t) = \dfrac{1}{2\pi}\displaystyle\int_0^{2\pi}\int_0^{\infty} q(1-\alpha_{12}q^2+\alpha_{22}D^2q^2)\widetilde{\widetilde{B_0}} \\ \qquad \Big(\dfrac{Fr\cos\psi}{2(D-Fr\cos\psi)}e^{-iqDt} - \dfrac{Fr\cos\psi}{2(D+Fr\cos\psi)}e^{iqDt}\Big)e^{iqr\cos(\psi-\theta)}dqd\psi \end{cases}. \tag{S.2.14}$$

The expressions in (S.2.14) are highly similar to the linear and fully dispersive solutions, (2.18) in the main paper. The only differences are the definition of D and the replacement of $1/\cosh(\mu q)$ with $1-\alpha_{12}q^2+\alpha_{22}D^2q^2$, which are expansions (approximations) of the fully dispersive solutions, as shown by Lo & Liu (2017) for the 1DH case.

The far-field and the far-field leading wave solutions can be sought from (S.2.14) using the same approaches discussed in Section 2 in the main paper. The far-field solutions read

$$\begin{aligned} \eta_{\text{far}} &= \frac{1}{\sqrt{2\pi}}r^{-\frac{1}{2}}\int_0^{\infty}(1-\alpha_{12}q^2+\alpha_{22}D^2q^2)\widetilde{\widetilde{B_0}}(q,\theta)\frac{Fr\cos\theta}{2(D-Fr\cos\theta)}q^{\frac{1}{2}}e^{i\left(q(r-Dt)-\frac{\pi}{4}\right)}dq \\ &\quad + \frac{1}{\sqrt{2\pi}}r^{-\frac{1}{2}}\int_0^{\infty}(1-\alpha_{12}q^2+\alpha_{22}D^2q^2)\widetilde{\widetilde{B_0}}(q,\pi+\theta)\frac{Fr\cos\theta}{2(D-Fr\cos\theta)}q^{\frac{1}{2}}e^{-i\left(q(r-Dt)-\frac{\pi}{4}\right)}dq \end{aligned}. \tag{S.2.15}$$

On the other hand, the far-field leading wave solutions are exactly the same as (2.22) in the main paper, since the far-field leading wave depends only on the leading-order frequency dispersion effect, which is captured in LWD.

S.3. Numerical solvers

Long-wave models are derived under the assumptions of an inviscid, incompressible, irrotational free surface flow where the characteristic length of the waves (which has been introduced before as L) is large compared to the water depth (which has been introduced before as d), i.e., $\mu = d/L \ll 1$. Within the context of long-wave theory, a moving bottom obstacle is interpreted as a changing bathymetry – the still water depth (i.e., the bathymetry) is allowed to vary in both space and time. The derivation of long-wave equations is well known, and can be found in many studies; e.g., Wei *et al.* (1995), Madsen & Schäffer (1998) and Madsen *et al.* (2002). Conventionally, the seafloor is regarded as stationary in time in modeling tsunamis. As a result, temporal derivatives of the bathymetry are omitted in the derivation of long-wave equations (e.g., the three above-mentioned studies). To study water waves generated by a deforming bottom boundary, it is therefore important to ensure that all necessary temporal derivatives are kept, as has been done in Lynett & Liu (2002), Fuhrman & Madsen (2009), Mitsotakis (2009), and Zhou & Teng (2010). Here we present the dimensionless mass and momentum equations in 2DH

adopted from Lynett & Liu (2002):

$$\frac{1}{\epsilon}H_t + \nabla\cdot\Big[H(\vec{u}_\alpha + \mu^2\vec{u}_1)\Big] = O(\mu^4), \tag{S.3.1}$$

and

$$\begin{aligned}
&\vec{u}_{\alpha,t} + \epsilon(\vec{u}_\alpha\cdot\nabla)\vec{u}_\alpha + \nabla\eta + \mu^2\left\{z_\alpha\nabla G_1 + \frac{1}{2}z_\alpha^2\nabla G_2\right\}_t \\
&+\epsilon\mu^2\left\{G_1\nabla G_1 - \nabla(\eta G_{1,t}) + \Big[\vec{u}_\alpha\cdot(\nabla z_\alpha)\Big](\nabla G_1 + z_\alpha\nabla G_2) + z_\alpha\nabla(\vec{u}_\alpha\cdot\nabla G_1) + \frac{1}{2}z_\alpha^2\nabla(\vec{u}_\alpha\cdot\nabla G_2)\right\}, \\
&+\epsilon^2\mu^2\nabla\left\{\eta G_1 G_2 - \eta\vec{u}_\alpha\cdot\nabla G_1 - \frac{1}{2}\eta^2 G_{2,t}\right\} + \epsilon^3\mu^2\nabla\left\{\frac{1}{2}\eta^2(G_2^2 - \vec{u}_\alpha\cdot\nabla G_2)\right\} = O(\mu^4)
\end{aligned} \tag{S.3.2}$$

where

$$G_1 = \nabla\cdot(h\vec{u}_\alpha) + \frac{1}{\epsilon}h_t, \qquad G_2 = \nabla\cdot\vec{u}_\alpha\ , \tag{S.3.3}$$

and

$$\vec{u}_1 = \left\{z_\alpha + \frac{1}{2}(h-\epsilon\eta)\right\}\nabla G_1 + \left\{\frac{1}{2}z_\alpha^2 - \frac{1}{6}\Big[(\epsilon\eta)^2 - \epsilon\eta h + h^2\Big]\right\}\nabla G_2. \tag{S.3.4}$$

We refer to (S.3.1) and (S.3.2) as FNWD (fully nonlinear and weakly dispersive wave model), which is accurate up to $O(\mu^2)$, has a truncation error of $O(\mu^4)$, and invokes no assumption on the wave nonlinearity ϵ.

In (S.3.1)–(S.3.4), consistent with the normalisation used in the main paper, the spatial variables (x, y) are normalised by L, the time variable t is normalised by $L/\sqrt{gd}$, and the free surface elevation η is normalised by A. The newly introduced variables are: the bathymetry (still water depth) h, which is normalised by d, and the total water depth H, which can be written as $H = h + \epsilon\eta$. In the bottom-obstacle-generated wave problem, the characteristic wave height is assumed to be the same as the characteristic bottom obstacle thickness A, and the characteristic wavelength is assumed to be the same as the characteristic bottom obstacle length L. In addition, it is convenient to isolate the bottom obstacle from the bathymetry, by writing

$$h(x, y, t) = h_0(x, y) - \epsilon B(x, y, t), \tag{S.3.5}$$

where $h_0(x, y)$ is the still water depth that does not change in time, and $B(x, y, t)$ is the bottom obstacle function. Within long-wave theory, $B(x, y, t)$ has to satisfy the scaling assumption in (S.3.1) and (S.3.2). Namely, B and its derivatives, normalised by L in length, A in height, and $L/\sqrt{gd}$ in time, are required to remain of order one. Therefore, an obstacle of a locally fast-varying shape (which results in locally large derivatives of B), such as a semi-ellipse, for which case the slope approaches infinity near the two ends, violates the scaling assumption and cannot be accurately resolved by long-wave models.

The leading-order flow velocity $\vec{u}_\alpha = (u_\alpha, v_\alpha)$, normalised by $\epsilon\sqrt{gd}$, is defined at a representative depth z_α, which can be chosen to improve frequency dispersion and maximise the accuracy of the long-wave equations (Nwogu 1993). For the best overall performance, Kennedy *et al.* (2001) and Shi *et al.* (2012) recommended the form

$$z_\alpha = \alpha h + \epsilon(1+\alpha)\eta, \quad \alpha = -0.531. \tag{S.3.6}$$

The full velocity distribution can be recovered as

$$\vec{U}(x, y, z, t) = \vec{u}_\alpha - \mu^2\left\{\frac{1}{2}(z^2 - z_\alpha^2)\nabla(\nabla\cdot\vec{u}_\alpha) + (z - z_\alpha)\nabla\left[\nabla\cdot(h\vec{u}_\alpha + \frac{h_t}{\epsilon})\right]\right\}, \tag{S.3.7}$$

where the terms multiplied by μ^2 are the higher-order velocity correction. After depth-averaging, the higher-order velocity correction becomes $\vec{u}_1 = (u_1, v_1)$, (S.3.4), which is normalised by $\epsilon\sqrt{gd}$ and of $O(1)$. However, it shows up in the equations as $\mu^2\vec{u}_1$.

In this study, FNWD is the most accurate, and therefore the most computationally expensive, long-wave model. By making further assumptions on μ^2 and ϵ, simpler and therefore less accurate and less expensive long-wave models can be obtained: neglecting the $\epsilon\mu^2$, $\epsilon^2\mu^2$, and $\epsilon^3\mu^2$ terms in (S.3.1) and (S.3.2) results in WNWD (weakly nonlinear and weakly dispersive wave model; commonly known as the extended Boussinesq equations), which has a truncation error of $O(\mu^4, \epsilon\mu^2)$; neglecting all terms involving μ^2 results in NSWE (nonlinear shallow water wave equations), which has a truncation error of $O(\mu^2)$; neglecting all terms involving ϵ results in LWD (linear and weakly dispersive wave model), which has a truncation error of $O(\mu^4, \epsilon)$; neglecting all terms involving ϵ or μ^2 results in LSWE (linear shallow water wave equations), which has a truncation error of $O(\mu^2, \epsilon)$. A scaling analysis can be performed to verify that the linear models are independent of the nonlinearity parameter ϵ (i.e., how thick the obstacle is), and the nondispersive models are independent of the frequency dispersion parameter μ (i.e., how shallow the water is).

Typically, to model a long-wave problem, one employs just one set of long-wave equations and develop a numerical solver for it. However, in this study, we utilise the different sets of long-wave equations to study the effects due to nonlinearity alone (i.e., the ϵ terms), frequency dispersion alone (i.e., the μ^2 terms), and nonlinear frequency dispersion (i.e., all terms altogether). For the same wave problem, comparing the results predicted by the different long-wave models enables the isolation of each of these effects. For example, comparing the LSWE results with the NSWE results reveals the effects due to nonlinearity alone; comparing the LSWE results with the LWD results reveals the effects due to frequency dispersion alone; comparing the NSWE results or the LWD results with the WNWD results or the FNWD results reveals the effects due to nonlinear frequency dispersion. In order to achieve this, a suite of comparable numerical solvers must be developed, so that these long-wave equations are arranged in similar forms and solved with comparable numerical accuracy. A similar analysis was performed by Lynett & Liu (2002) for landslide-generated waves in 1DH; in this study, we perform such an analysis in 2DH, with a focus on examining the deviations from the linear analytical solutions.

S.3.1. *Numerical methods*

In this study, two types of numerical solvers are developed: one for the linear long-wave equations, LSWE and LWD, and the other for the nonlinear long-wave equations, NSWE, WNWD, and FNWD. The linear equation solver adopts a finite-difference framework, using the fourth-order central difference method to discretise in space, and the third-order SSP-RK (Gottlieb *et al.* 2001) to march in time. The nonlinear equation solver adopts a hybrid finite-difference/finite-volume shock-capturing scheme, using either the second-order MUSCL (Toro 2001) or the fifth-order WENO (Jiang & Shu 1996) to discretise in space, and the third-order SSP-RK (Gottlieb *et al.* 2001) to march in time. The dimensional equations are solved. No model tuning, such as the bottom friction and wave breaking dissipation terms, is introduced.

The numerical solution of long-wave equations is considered a mature research subject, on which many studies exist: for example, Toro (2001), Li & Raichlen (2002), Lynett & Liu (2002), Wei *et al.* (2006), Shiach & Mingham (2009), Shi *et al.* (2012), Dutykh & Kalisch (2013), Zhou *et al.* (2016), and Hatland & Kalisch (2019). Therefore, we only briefly outline the governing equations and the numerical methods of our numerical solvers in Section S.3.1.1 for the linear long-wave numerical models, and in Section S.3.1.2 for the nonlinear long-wave numerical models.

S.3.1.1. *Linear long-wave numerical models*

In the linear long-wave models, the nonlinear terms in (S.3.1) and (S.3.2), i.e., terms multiplied with ϵ, are omitted. Using primes to denote dimensional quantities, we rearrange the dimensional mass and momentum equations for the linear long-wave models to be

$$\begin{cases} \eta'_{t'} + \left[h'_0(u'_\alpha + u'_1)\right]_{x'} + \left[h'_0(v'_\alpha + v'_1)\right]_{y'} = B'_{t'}, \\ (u'_\alpha + u'_2)_{t'} = -g\eta'_{x'}, \quad (v'_\alpha + v'_2)_{t'} = -g\eta'_{y'}, \end{cases} . \tag{S.3.8}$$

For LSWE, $u'_1 = u'_2 = v'_1 = v'_2 = 0$. For LWD,

$$\begin{cases} u'_1 = (z'_\alpha + \frac{1}{2}h'_0)G'_{1,x'} + (\frac{1}{2}z'^2_\alpha - \frac{1}{6}h'^2_0)G'_{2,x'}, \quad u'_2 = z'_\alpha G'_{1,x'} + \frac{1}{2}z'^2_\alpha G'_{2,x'} \\ v'_1 = (z'_\alpha + \frac{1}{2}h'_0)G'_{1,y'} + (\frac{1}{2}z'^2_\alpha - \frac{1}{6}h'^2_0)G'_{2,y'}, \quad v'_2 = z'_\alpha G'_{1,y'} + \frac{1}{2}z'^2_\alpha G'_{2,y'} \\ z'_\alpha = \alpha h'_0, \quad \alpha = -0.531 \\ G'_1 = (h'_0 u'_\alpha)_{x'} + (h'_0 v'_\alpha)_{y'} + h'_{t'}, \quad G'_2 = u'_{\alpha,x'} + v'_{\alpha,y'} \end{cases} . \tag{S.3.9}$$

We recall that $h'_0(x', y')$ is the bathymetry that excludes the bottom obstacle, and $h'(x', y', t') = h'_0(x', y') - B'(x', y', t')$ is the bathymetry that includes it. While u'_1 and v'_1 are the depth-averaged higher-order velocity corrections, u'_2 and v'_2 do not have physical meanings.

A finite-difference scheme, the same as that used in Lo & Liu (2017) for solving LSWE, is employed. The fourth-order central difference scheme is used for the spatial discretisation, and the third-order Strong Stability Preserving Runge-Kutta (SSP-RK; see Gottlieb *et al.* 2001) is used for the time marching.

At each iteration in time based on the SSP-RK scheme, η', $P' = (u'_\alpha + u'_2)$, and $Q' = (v'_\alpha + v'_2)$ are updated via equations (S.3.8). While $u'_\alpha = P'$ and $v'_\alpha = Q'$ can be recovered directly in LSWE since $u'_2 = v'_2 = 0$, a matrix system needs to be solved for each velocity component in LWD, since u'_2 and v'_2 depend on u'_α and v'_α. This process is briefly explained here for u'_α: writing u'_2 in (S.3.9) out fully gives

$$u'_2 = z'_\alpha(h'_0 u'_\alpha)_{x'x'} + z'_\alpha(h'_0 v'_\alpha)_{y'x'} + z'_\alpha h'_{t'x'} + \frac{1}{2}z'^2_\alpha u'_{\alpha,x'x'} + \frac{1}{2}z'^2_\alpha v'_{\alpha,y'x'}. \tag{S.3.10}$$

Separating the terms with u'_α from those with v'_α results in

$$N'_1 = z'_\alpha(h'_0 u'_\alpha)_{x'x'} + \frac{1}{2}z'^2_\alpha u'_{\alpha,x'x'}, \quad N'_2 = z'_\alpha(h'_0 v'_\alpha)_{y'x'} + \frac{1}{2}z'^2_\alpha v'_{\alpha,y'x'} + z'_\alpha h'_{t'x'}. \tag{S.3.11}$$

Using $\Delta x'$ to denote the grid spacing in x' and i to denote the index for x' in the numerical model, we employ the second-order central difference formula to discretise N'_1 as

$$N'_{1,i} = z'_{\alpha,i}\frac{(h'_0 u'_\alpha)_{i+1} - 2(h'_0 u'_\alpha)_i + (h'_0 u'_\alpha)_{i-1}}{\Delta x'^2} + \frac{1}{2}z'^2_{\alpha,i}\frac{u'_{\alpha,i+1} - 2u'_{\alpha,i} + u'_{\alpha,i-1}}{\Delta x'^2}. \tag{S.3.12}$$

On the other hand, N'_2 is independent of u'_α. The fourth-order central difference scheme and v'_α from the previous sub-time step are used to compute N'_2. $P' = u'_\alpha + u'_2 = u'_\alpha + N'_1 + N'_2$ can be rearranged to be $u'_\alpha + N'_1 = P' - N'_2$, for which a matrix system with discretised N'_1 can be set up to solve for u'_α. A similar matrix is set up and solved for v'_α.

S.3.1.2. *Nonlinear long-wave numerical models*

The nonlinear long-wave equations – NSWE, WNWD, and FNWD – are solved by using a hybrid finite-volume/finite-difference shock-capturing numerical scheme. The spatial accuracy can be either second-order (MUSCL with a van Leer slope limiter; see Toro 2001) for quicker computation, or fifth-order accurate (WENO; see Jiang & Shu 1996), and the temporal accuracy is third-order (SSP-RK; see Gottlieb *et al.* 2001). The local Riemann problem is solved by an HLLC

approximate Riemann solver (Toro 2001), which is applicable to both wet-wet cell interfaces and wet-dry cell interfaces. An advantage of employing a Riemann solver is that the shoreline, a wet-dry cell interface, is automatically captured without additional numerical treatment. In recent years, shock-capturing numerical schemes have become a robust and standard means for solving long-wave equations; see e.g., Li & Raichlen (2002), Wei *et al.* (2006), Shiach & Mingham (2009), Shi *et al.* (2012), and Zhou *et al.* (2016). The main distinguishing features of our numerical model are the formal allowance, i.e., the bathymetry is allowed to vary in time in the derivation of the governing equations, of a bathymetry that changes appreciably in time, and the easiness in switching between solving the different long-wave models.

After substantial rearrangement of (S.3.1) and (S.3.2) into a form suitable for the numerical solver, the dimensional mass equation in 2DH reads:

$$H'_{t'} + \left[H'(u'_\alpha + u'_1)\right]_{x'} + \left[H'(v'_\alpha + v'_1)\right]_{y'} = 0, \tag{S.3.13}$$

and the dimensional momentum equations in 2DH read:

$$\begin{cases} \left[H'(u'_\alpha + u'_2)\right]_{t'} + \left[H'(u'_\alpha + u'_1)'^2 + \dfrac{1}{2}g(\eta'^2 + 2\eta' h')\right]_{x'} + \left[H'(u'_\alpha + u'_1)(v'_\alpha + v'_1)\right]_{y'} \\ \qquad\qquad = g\eta' h'_{x'} + S'_X \\ \left[H'(v'_\alpha + v'_2)\right]_{t'} + \left[H'(u'_\alpha + u'_1)(v'_\alpha + v'_1)\right]_{x'} + \left[H'(v'_\alpha + v'_1)'^2 + \dfrac{1}{2}g(\eta'^2 + 2\eta' h')\right]_{y'} \\ \qquad\qquad = g\eta' h'_{y'} + S'_Y \end{cases}. \tag{S.3.14}$$

For NSWE, $u'_1 = u'_2 = v'_1 = v'_2 = S'_X = S'_Y = 0$. For WNWD,

$$\begin{cases} u'_1 = (z'_\alpha + \dfrac{1}{2}h')G'_{1,x'} + (\dfrac{1}{2}z'^2_\alpha - \dfrac{1}{6}h'^2)G'_{2,x'}, \quad u'_2 = z'_\alpha G'_{1,x'} + \dfrac{1}{2}z'^2_\alpha G'_{2,x'} \\ v'_1 = (z'_\alpha + \dfrac{1}{2}h')G'_{1,y'} + (\dfrac{1}{2}z'^2_\alpha - \dfrac{1}{6}h'^2)G'_{2,y'}, \quad v'_2 = z'_\alpha G'_{1,y'} + \dfrac{1}{2}z'^2_\alpha G'_{2,y'} \\ S'_X = H'_{t'}(u'_2 - u'_1), \quad S'_Y = H'_{t'}(v'_2 - v'_1) \\ z'_\alpha = \alpha h', \quad \alpha = -0.531 \\ G'_1 = (h'u'_\alpha)_{x'} + (h'v'_\alpha)_{y'} + h'_{t'}, \quad G'_2 = u'_{\alpha,x'} + v'_{\alpha,y'}. \end{cases} \tag{S.3.15}$$

For FNWD,

$$
\begin{cases}
u_1' = (z_\alpha' + \frac{1}{2}h' - \frac{1}{2}\eta')G_{1,x'}' + (\frac{1}{2}z_\alpha'^2 - \frac{1}{6}h'^2 - \frac{1}{6}\eta'^2 + \frac{1}{6}\eta' h')G_{2,x'}' \\
u_2' = z_\alpha' G_{1,x'}' + \frac{1}{2}z_\alpha'^2 G_{2,x'}' - (\eta' G_1' + \frac{1}{2}\eta'^2 G_2')_{x'} \\
v_1' = (z_\alpha' + \frac{1}{2}h' - \frac{1}{2}\eta')G_{1,y'}' + (\frac{1}{2}z_\alpha'^2 - \frac{1}{6}h'^2 - \frac{1}{6}\eta'^2 + \frac{1}{6}\eta' h')G_{2,y'}' \\
v_2' = z_\alpha' G_{1,y'}' + \frac{1}{2}z_\alpha'^2 G_{2,y'}' - (\eta' G_1' + \frac{1}{2}\eta'^2 G_2')_{y'} \\
S_X' = H_{t'}'(u_2' - u_1') + H'\Big\{(u_1' u_{\alpha,x'}' + v_1' u_{\alpha,y'}' + u_\alpha' u_{1,x'}' + v_\alpha' u_{1,y'}') - \Big[\eta_{t'}'(G_1' + \eta' G_2')\Big]_{x'} \\
\qquad -\Big[G_1' G_{1,x'}' + (u_\alpha' z_{\alpha,x'}' + v_\alpha' z_{\alpha,y'}')(G_{1,x'}' + z_\alpha' G_{2,x'}') + z_\alpha'(u_\alpha' G_{1,x'}' + v_\alpha' G_{1,y'}')_{x'} \\
\qquad\qquad +\frac{1}{2}z_\alpha'^2(u_\alpha' G_{2,x'}' + v_\alpha' G_{2,y'}')_{x'}\Big] \\
\qquad -\Big[\eta'(G_1' G_2' - u_\alpha' G_{1,x'}' - v_\alpha' G_{1,y'}')\Big]_{x'} - \frac{1}{2}\Big[\eta'^2(G_2'^2 - u_\alpha' G_{2,x'}' - v_\alpha' G_{2,y'}')\Big]_{x'}\Big\} \\
S_Y' = H_{t'}'(v_2' - v_1') + H'\Big\{(u_1' v_{\alpha,x'}' + v_1' v_{\alpha,y'}' + u_\alpha' v_{1,x'}' + v_\alpha' v_{1,y'}') - \Big[\eta_{t'}'(G_1' + \eta' G_2')\Big]_{y'} \\
\qquad -\Big[G_1' G_{1,y'}' + (u_\alpha' z_{\alpha,x'}' + v_\alpha' z_{\alpha,y'}')(G_{1,y'}' + z_\alpha' G_{2,y'}') + z_\alpha'(u_\alpha' G_{1,x'}' + v_\alpha' G_{1,y'}')_{y'} \\
\qquad\qquad +\frac{1}{2}z_\alpha'^2(u_\alpha' G_{2,x'}' + v_\alpha' G_{2,y'}')_{y'}\Big] \\
\qquad -\Big[\eta(G_1' G_2' - u_\alpha' G_{1,x'}' - v_\alpha' G_{1,y'}')\Big]_{y'} - \frac{1}{2}\Big[\eta'^2(G_2'^2 - u_\alpha' G_{2,x'}' - v_\alpha' G_{2,y'}')\Big]_{y'}\Big\} \\
z_\alpha' = \alpha h' + (1+\alpha)\eta', \quad \alpha = -0.531 \\
G_1' = (h' u_\alpha')_{x'} + (h' v_\alpha')_{y'} + h_{t'}', \quad G_2' = u_{\alpha,x'}' + v_{\alpha,y'}'
\end{cases}
\tag{S.3.16}
$$

Similarly to the linear long-wave models, while u_1' and v_1' are the depth-averaged higher-order velocity corrections, u_2' and v_2' do not have physical meanings. We recall that $H'(x', y', t') = \eta'(x', y', t') + h'(x', y', t')$ is the total water depth, and the bathymetry $h'(x', y', t')$ can be expressed as $h'(x', y', t') = h_0'(x', y') - B'(x', y', t')$ to separate the still water bathymetry h_0' from the bottom obstacle B'.

At each iteration in time based on the SSP-RK scheme, H' in (S.3.13) and $P' = H'(u_\alpha' + u_2')$ and $Q' = H'(v_\alpha' + v_2')$ in (S.3.14) are updated using Godunov's scheme (see e.g., Toro 2001). The spatial derivatives in the expressions for u_1', u_2', v_1', v_2', S_X', S_Y', and the terms $g\eta' h_{x'}'$ and $g\eta' h_{y'}'$ on the right hand sides of (S.3.14), are calculated by the fourth-order central difference formula. The temporal derivatives (i.e., $\eta_{t'}'$, and $B_{t'}'$ if an analytical expression for the obstacle function is not available) in the expressions for G_1', S_X', and S_Y', are calculated with a two-point difference formula using the values stored at each sub-time step in the SSP-RK time-updating scheme. More detailed discussions can be found in Shi *et al.* (2012).

While u_α' and v_α' can be directly recovered in NSWE, a matrix system needs to be solved for each velocity component in FNWD and WNWD, since u_2' and v_2' are functions of u_α' and v_α'. Here we briefly explain the process for u_α': writing u_2' in (S.3.16) out fully yields

$$
\begin{aligned}
u_2' = {} & z_\alpha'(h' u_\alpha')_{x'x'} + z_\alpha'(h' v_\alpha')_{y'x'} + z_\alpha' h_{t'x'}' + \frac{1}{2}z_\alpha'^2 u_{\alpha,x'x'}' + \frac{1}{2}z_\alpha'^2 v_{\alpha,y'x'}' \\
& - C_{\mathrm{FNWD}}\Big[\eta_{x'}'(h' u_\alpha')_{x'} + \eta_{x'}'(h' v_\alpha')_{y'} + \eta_{x'}' h_{t'}' + \eta'(h' u_\alpha')_{x'x'} + \eta'(h' v_\alpha')_{y'x'} \\
& \qquad + \eta' h_{t'x'}' + \eta'\eta_{x'}' u_{\alpha,x'}' + \eta'\eta_{x'}' v_{\alpha,y'}' + \frac{1}{2}\eta'^2 u_{\alpha,x'x'}' + \frac{1}{2}\eta'^2 v_{\alpha,y'x'}'\Big]
\end{aligned}
\tag{S.3.17}
$$

where $C_{\mathrm{FNWD}} = 1$ for FNWD and $C_{\mathrm{FNWD}} = 0$ for WNWD. Separating the terms with u'_α from those with v'_α gives

$$\begin{aligned} N'_1 &= z'_\alpha (h'u'_\alpha)_{x'x'} + \frac{1}{2} z'^2_\alpha u'_{\alpha,x'x'x'} \\ &\quad - C_{\mathrm{FNWD}} \left[\eta'_{x'} (h'u'_\alpha)_{x'} + \eta' (h'u'_\alpha)_{x'x'} + \eta' \eta'_{x'} u'_{\alpha,x'} + \frac{1}{2} \eta'^2 u'_{\alpha,x'x'} \right] \\ N'_2 &= z'_\alpha (h'v'_\alpha)_{y'x'} + \frac{1}{2} z'^2_\alpha v'_{\alpha,y'x'} + z'_\alpha h'_{t'x'} \\ &\quad - C_{\mathrm{FNWD}} \left[\eta'_{x'} (h'v'_\alpha)_{y'} + \eta' (h'v'_\alpha)_{y'x'} + \eta' \eta'_{x'} v'_{\alpha,y'} + \frac{1}{2} \eta'^2 v'_{\alpha,y'x'} + \eta'_{x'} h'_{t'} + \eta' h'_{t'x'} \right] \end{aligned} . \quad \text{(S.3.18)}$$

With $\Delta x'$ denoting the grid spacing in x' and i denoting the index for x' in the numerical model, the second-order central difference formula can be employed to discretise N'_1 as

$$\begin{aligned} N'_{1,i} &= z'_{\alpha,i} \frac{(h'u'_\alpha)_{i+1} - 2(h'u'_\alpha)_i + (h'u'_\alpha)_{i-1}}{\Delta x'^2} + \frac{1}{2} z'^2_{\alpha,i} \frac{u'_{\alpha,i+1} - 2u'_{\alpha,i} + u'_{\alpha,i-1}}{\Delta x'^2} \\ &\quad - C_{\mathrm{FNWD}} \left[\eta'_{x'} \frac{(h'u'_\alpha)_{i+1} - (h'u'_\alpha)_{i-1}}{2\Delta x'} + \eta' \frac{(h'u'_\alpha)_{i+1} - 2(h'u'_\alpha)_i + (h'u'_\alpha)_{i-1}}{\Delta x'^2} \right. \\ &\quad \left. + \eta' \eta'_{x'} \frac{u'_{\alpha,i+1} - u'_{\alpha,i-1}}{2\Delta x'} + \frac{1}{2} \eta'^2 \frac{u'_{\alpha,i+1} - 2u'_{\alpha,i} + u'_{\alpha,i-1}}{\Delta x'^2} \right] \end{aligned} . \quad \text{(S.3.19)}$$

On the other hand, N'_2 is independent of u'_α. The fourth-order central difference scheme and v'_α from the previous sub-time step are used to compute N'_2. $P' = H'(u'_\alpha + u'_2) = H'(u'_\alpha + N'_1 + N'_2)$ can be rearranged to be $u'_\alpha + N'_1 = P'/H' - N'_2$, for which a matrix system with discretised N'_1 can be set up to solve for u'_α. A similar procedure is repeated to solve for v'_α.

S.3.2. *Validation*

Long-wave models are known to be accurate when the scaling assumptions are met, and shock-capturing numerical schemes have been found to be an effective way of solving them (see e.g., Li & Raichlen 2002; Wei *et al.* 2006; Shiach & Mingham 2009; Shi *et al.* 2012; Kazolea *et al.* 2012; Zhou *et al.* 2016). Several benchmark tests have been performed using our numerical model (Lo 2018). These tests include: 1DH regular waves traveling over a submerged dike (Beji & Battjes 1993; Dingemans 1994), 1DH solitary wave runup on a slope (Synolakis 1987), 2DH solitary wave runup on a conical island (Liu *et al.* 1995), 1DH bottom-obstacle-generated waves in constant depth (Whittaker *et al.* 2015, 2017), and 1DH bottom-obstacle-generated waves on a slope (Zhou & Teng 2010; Sue *et al.* 2011).

In this study, only benchmark tests involving a moving bottom obstacle are relevant. Perhaps due to the difficulty in realising the long physical lengths in the laboratory, 2DH laboratory experiments on bottom-obstacle-generated waves satisfying the long-wave assumptions are limited. As remarked by Zhou & Teng (2010), while many 2DH laboratory experiments on solid-landslide-generated waves have been conducted (e.g., Liu *et al.* 2005; Panizzo *et al.* 2005; Enet & Grilli 2007; Di Risio *et al.* 2009; Lindstrøm *et al.* 2014; Romano *et al.* 2016), weakly dispersive long-wave models cannot be expected to be applicable to these cases, due to the relatively short landslide and/or the sharp landslide shapes used. There are also laboratory experiments on granular-landslide-generated waves (e.g., Fritz *et al.* 2004; Heller & Hager 2010; Mohammed & Fritz 2012; McFall & Fritz 2016). However, granular materials require different modeling techniques, which are beyond the current capability of our numerical model. 3D CFD (Computational Fluid Dynamics) or nonhydrostatic models may be necessary for predicting water waves generated by a deformable subaerial landslide (see e.g., Ma *et al.* 2015, Kim *et al.* 2020 and Hu *et al.* 2020). As a result of the above-mentioned reasons, only 1DH bottom-obstacle-generated wave benchmark tests have been performed.

The most relevant benchmark test is Whittaker *et al.* (2017)'s 1DH experiments involving water

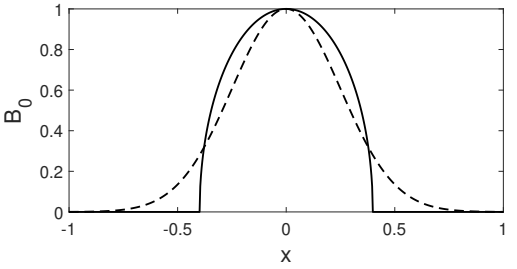

Figure 1: The semi-elliptical obstacle (solid line) used in Whittaker *et al.* (2017)'s laboratory experiments and CFD simulations compared with the Gaussian-shaped obstacle (dashed line) used in our long-wave numerical models. The two shapes enclose the same area. The maximum thickness of the obstacle is used to normalise B_0, and the characteristic length of the Gaussian shape, $L \simeq 0.627$ m, is used to normalise x.

waves generated by a moving bottom obstacle in a constant water depth of $d = 0.175$ m. A semi-elliptical bottom obstacle of length 0.5 m and height 0.026 m was used in the experiments. Since a semi-ellipse has discontinuities at the two edges and cannot be accurately resolved by long-wave models, a Gaussian-shaped landslide of the same height $A = 0.026$ m and enclosed area is used in the numerical simulations. The resulting Gaussian-shaped obstacle has a characteristic length scale $L = 0.5\sqrt{\pi/2} \simeq 0.627$ m based on the shape definition (2.28) in the main paper. The two shapes are compared in figure 1.

In the case considered, the bottom obstacle accelerates for a dimensionless duration of $t_{\text{acc}} = 0.913$ (we recall that time is normalised by $L/\sqrt{gd}$) until it reaches a constant normalised speed of Fr. The obstacle then travels at a constant normalised speed of Fr for a dimensionless duration of $t_{Fr} = 4.18$, before decelerating to a halt over a dimensionless duration of $t_{\text{dec}} = 0.913$. The experimental data and the numerical results are compared in figure 2 at three different times, $t = 2, 6, 10$. The FNWD results are computed using the fifth-order accurate WENO scheme, with $\Delta x = 0.05$ (normalised by L). The CFD results from Whittaker *et al.* (2017) are also included. CFD makes no assumptions on the scales of the water waves, and the actual semi-elliptical obstacle shape can be used.

As shown in figure 2, the results for the leading waves compare well. There are actually two leading waves – one propagates in the negative x direction, and the other propagates in the positive x direction. For brevity, we focus only on the leading wave in the positive x direction, as the waves in this direction are larger and therefore more visible in the figure. Consistent with the analytical findings derived in Section 2 in the main paper and long-wave theory in general, the leading wave has the longest wavelength. Behind it exist oscillatory trailing waves. While these trailing waves have noticeably shorter wavelengths, their amplitudes are comparable to that of the leading wave. Discrepancies between the results occur mostly in the trailing waves. Nonetheless, the overall characteristics are fairly similar. At least for the leading waves, which are our primary interest, this benchmark test suggests that the long-wave assumptions are met in this experiment, and that the results calculated by our numerical solver are trustworthy.

S.3.3. *Verification*

Since there are no suitable experimental data for validating our numerical results for bottom-obstacle-generated water waves in 2DH, we rely on verification tests to gain confidence in the numerical results. For a bottom obstacle translating at a constant speed, integral-form analytical solutions can be obtained for LSWE and LWD (the derivation for LWD is outlined in Section S.2). Thus, the performance of the linear long-wave models can be easily verified. As examples, the analytical solutions are compared with the numerical results in figure 3 for LSWE, and in figure 4

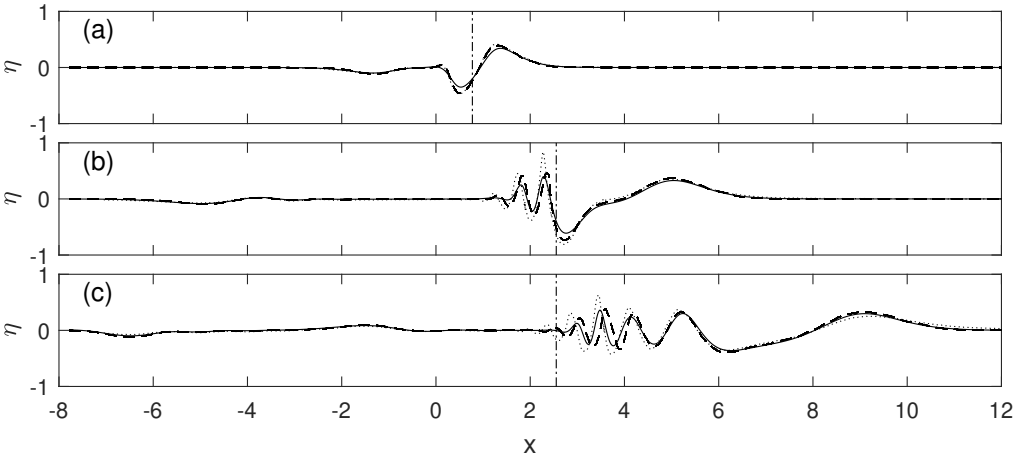

Figure 2: The free surface elevations predicted by different numerical models compared with Whittaker *et al.* (2017)'s experimental data. Solid line: FNWD using an approximate obstacle shape; dashed line: CFD (from Whittaker *et al.* 2017) using the actual obstacle shape; dotted line: experimental data; dash-dot line: the crest location of the bottom obstacle. (a) $t = 2$; (b) $t = 6$; (c) $t = 10$.

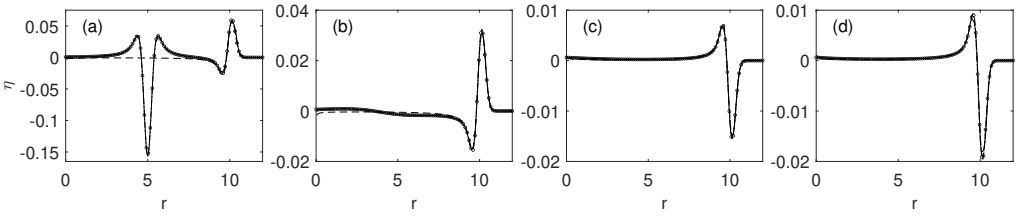

Figure 3: The linear and nondispersive free surface elevations predicted by different wave models plotted along four different directions at $t = 10$, with $Fr = 0.5$ and the Gaussian-shaped B_0 given in (2.28) in the main paper. Solid line: numerical results based on FNWD with $\epsilon = 0.01$ and $\mu = 0.01$; dash-dot line: numerical results based on LSWE; circle: the LSWE analytical solution, (2.18) in the main paper with $\mu \to 0$; dashed line: the far-field shallow water solution (2.32) in the main paper, accurate for large r. (a): $\theta = 0$; (b): $\theta = \pi/4$; (c): $\theta = 3\pi/4$; (d): $\theta = \pi$.

for LWD, at the instant $t = 10$. Whereas the LSWE results compare well, the LWD results shows some discrepancy in the trailing waves. These trailing waves can be very short and oscillatory – the wavelengths can be as short as roughly one tenth of that of the leading wave in figure 4. As a result, very high (higher than the present grid spacing, $\Delta x = \Delta y = 0.05$) grid resolution is needed to accurately capture all trailing waves. As our primary interest is in the leading long waves, we neither seek nor expect to capture the short trailing waves; the results for the leading long waves all agree nearly perfectly.

In addition, as another means of verification, long-wave models should converge to one another in the right scaling limits. For example, if a very thin obstacle is used so that $\epsilon \to 0$, the NSWE results should converge to the LSWE results, and the FNWD or WNWD results should converge to the LWD results. Similarly, if a very long obstacle is used so that $\mu \to 0$, the LWD results should converge to the LSWE results, and the FNWD or WNWD results should converge to the NSWE results. Lastly, if a very thin and very long obstacle is used so that $\epsilon \to 0$ and $\mu \to 0$, the FNWD or WNWD results should converge to the LSWE results. In figure 3, this is verified for FNWD with $\epsilon = 0.01$ and $\mu = 0.01$; the FNWD results indeed converge to the LSWE results. In

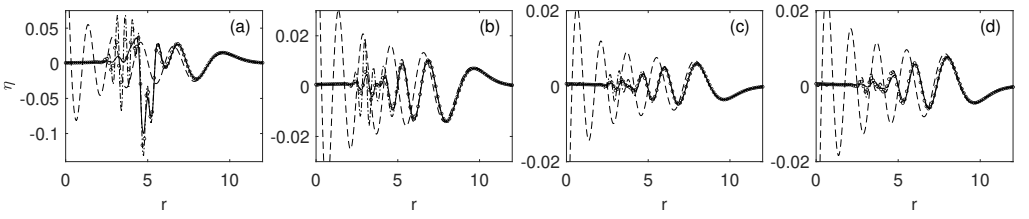

Figure 4: The linear and dispersive free surface elevations predicted by different wave models plotted along four different directions at $t = 10$, with $Fr = 0.5$, $\mu = 0.3$ and the Gaussian-shaped B_0 given in (2.28) in the main paper. Solid line: numerical results based on FNWD with $\epsilon = 0.01$; dash-dot line: numerical results based on LWD; circle: the LWD analytical solution (S.2.14); dashed line: the first term of the far-field leading wave solution (2.22) in the main paper, accurate for large r and near $r = t$. (a): $\theta = 0$; (b): $\theta = \pi/4$; (c): $\theta = 3\pi/4$; (d): $\theta = \pi$.

figure 4, this is verified for FNWD with $\mu = 0.01$; the FNWD results indeed converge to the LWD results. Small discrepancy in the amplitudes can be seen in the trailing waves. This is likely due to the numerical dissipation inherent in MUSCL-type numerical schemes – to save on computation time in 2DH, the second-order accurate MUSCL scheme with grid spacing $\Delta x = \Delta y = 0.05$ was used in the nonlinear long-wave model solvers. Again, since our primary interest is in the leading long waves, we do not seek to accurately capture all trailing waves; the results for the leading long waves all agree nearly perfectly.

REFERENCES

Beji, S. & Battjes, J.A. 1993 Experimental investigations of wave propagation over a bar. *Coast. Eng.* **19**, 151–162.

Di Risio, M., Bellotti, G., Panizzo, A. & De Girolamo, P. 2009 Three-dimensional experiments on landslide generated waves at a sloping coast. *Coast. Eng.* **56**, 659–671.

Dingemans, M. W. 1994 Comparison of computations with Boussinesq-like models and laboratory measurements. *Technical Report H1684.12 at Delft Hydraulics* .

Dutykh, D. & Kalisch, H. 2013 Boussinesq modeling of surface waves due to underwater landslides. *Nonlin. Processes Geophys.* **20**, 267–285.

Enet, F. & Grilli, S. T. 2007 Experimental study of tsunami generation by three-dimensional rigid underwater landslides. *J. Waterw. Port, Coast. Ocean Eng.* **133**, 442–454.

Fritz, H. M., Hager, W. H. & Minor, H.-E. 2004 Near field characteristic of landslide generated impulse waves. *J. Waterw. Port, Coast. Ocean Eng.* **130**, 187–302.

Fuhrman, D. R. & Madsen, P. A. 2009 Tsunami generation, propagation, and run-up with a high-order Boussinesq model. *Coastal Eng.* **56**, 747–758.

Gottlieb, S., Shu, C.-W. & Tadmor, E. 2001 Strong stability-preserving high-order time discretization methods. *SIAM Rev.* **43(1)**, 89–112.

Hatland, S. D. & Kalisch, H. 2019 Wave breaking in undular bores generated by a moving weir. *Phys. Fluids* **31**, 033601.

Heller, V. & Hager, W. H. 2010 Impulse product parameter in landslide generated impulse waves. *J. Waterw. Port, Coast. Ocean Eng.* **136(3)**, 145–155.

Hu, Y., Yu, Z. & Zhou, J. 2020 Numerical simulation of landslide-generated waves during the 11 October 2018 Baige landslide at the Jinsha River. *Landslides* .

Jiang, G.-S. & Shu, C.-W. 1996 Efficient implementation of weighted ENO schemes. *J. Comput. Phys.* **126**, 202–228.

Kazolea, M., Delis, A. I., Nikolos, I. K. & Synolakis, C. E. 2012 An unstructured finite volume numerical scheme for extended 2D Boussinesq-type equations. *Coast. Eng.* **69**, 42–66.

Kennedy, A. B., Kirby, J. T., Chen, Q. & Dalrymple, R. A. 2001 Boussinesq-type equations with improved nonlinear performance. *Wave Motion* **33**, 225–243.

Kim, G.-B., Cheng, W., Sunny, R. C., Horrillo, J. J., McFall, B. C., Mohammed, F., Fritz, H. M., Beget,

J. & Kowalik, Z. 2020 Three dimensional landslide generated tsunamis: Numerical and physical model comparisons. *Landslides* **17**, 1145–1161.

Li, Y. & Raichlen, F. 2002 Non-breaking and breaking solitary runup. *J. Fluid Mech.* **456**, 295–318.

Lindstrøm, E., Pedersen, G., Jensen, A. & Glimsdal, S. 2014 Experiments on slide generated waves in a 1:500 scale fjord model. *Coast. Eng.* **92**, 12–23.

Liu, P. L.-F., Cho, Y.-S., Briggs, M. J., Kanoglu, U. & Synolakis, C. E. 1995 Runup of solitary waves on a circular island. *J. Fluid Mech.* **302**, 259–289.

Liu, P. L.-F., Wu, T.-R., Raichlen, F., Synolakis, C. E. & Borrero, J. 2005 Runup and rundown generated by three-dimensional sliding masses. *J. Fluid Mech.* **536**, 107–144.

Lo, H.-Y. 2018 Modeling landslide-generated tsunamis with long-wave equations. PhD thesis, Cornell University.

Lo, H.-Y. & Liu, P. L.-F. 2017 On the analytical solutions for water waves generated by a prescribed landslide. *J. Fluid Mech.* **821**, 85–116.

Lynett, P. & Liu, P. L.-F. 2002 A numerical study of submarine-landslide-generated waves and run-up. *Proc. R. Soc. Lond.* **A 458**, 2885–2910.

Ma, G., Kirby, J. T., Hsu, T.-J. & Shi, F. 2015 A two-layer granular landslide model for tsunami wave generation: Theory and computation. *Ocean Model.* **93**, 40–55.

Madsen, P. A., Bingham, H. B. & Liu, H. 2002 A new Boussinesq method for fully nonlinear waves from shallow to deep water. *J. Fluid Mech.* **462**, 1–30.

Madsen, P. A. & Schäffer, H. A. 1998 Higher-order Boussinesq-type equations for surface gravity waves: derivation and analysis. *Proc. R. Soc. Lond.* **A 356**, 3123–3184.

McFall, B. C. & Fritz, H. M. 2016 Physical modelling of tsunamis generated by three-dimensional deformable granular landslides on planar and conical island slopes. *Proc. R. Soc. A.472 20160052* **472**, 20160052.

Mitsotakis, D. E. 2009 Boussinesq systems in two space dimensions over a variable bottom for the generation and propagation of tsunami waves. *Math. Comput. Simul.* **80**, 860–873.

Mohammed, F. & Fritz, H. M. 2012 Physical modeling of tsunamis generated by three-dimensional deformable granular landslides. *J. Geophys. Res.* **117**, C11015.

Nwogu, O. 1993 Alternative form of Boussinesq equations for nearshore wave propagation. *J. Waterw. Port, Coast. Ocean Eng.* **119(6)**, 618–638.

Panizzo, A., De Girolamo, P. & Petaccia, A. 2005 Forecasting impulse waves generated by subaerial landslides. *J. Geophys. Res.* **110**, C12025.

Romano, A., Di Risio, M., Bellotti, G., Molfetta, M. G., Damiani, L. & De Girolamo, P. 2016 Tsunamis generated by landslides at the coast of conical islands: experimental benchmark dataset for mathematical model validation. *Landslides* **13**, 1379–1393.

Shi, F., Kirby, J. T., Harris, J. C., Geiman, J. D. & Grilli, S. T. 2012 A high-order adaptive time-stepping TVD solver for Boussinesq modeling of breaking waves and coastal inundation. *Ocean Model.* **43–44**, 36–51.

Shiach, J. B. & Mingham, C. G. 2009 A temporally second-order accurate Godunov-type scheme for solving the extended Boussinesq equations. *Coast. Eng.* **56**, 32–45.

Sue, L. P., Nokes, R. I. & Davidson, M. J. 2011 Tsunami generation by submarine landslides: comparison of physical and numerical models. *Environ. Fluid Mech.* **11**, 133–165.

Synolakis, C. E. 1987 The runup of solitary waves. *J. Fluid Mech.* **185**, 523–545.

Toro, E. F. 2001 *Shock-capturing methods for free-surface shallow flows*. Wiley.

Wei, G., Kirby, J. T., Grilli, S. T. & Subramanya, R. 1995 A fully nonlinear Boussinesq model for surface waves. Part 1. Highly nonlinear unsteady waves. *J. Fluid Mech.* **294**, 71–92.

Wei, Y., Mao, X. Z. & Cheung, K. F. 2006 Well-balanced finite-volume model for long-wave runup. *J. Waterw. Port, Coast. Ocean Eng.* **132**, 114–124.

Whittaker, C. N., Nokes, R. I. & Davidson, M. J. 2015 Tsunami forcing by a low Froude number landslide. *Environ. Fluid Mech.* **15(6)**, 1215–1239.

Whittaker, C. N., Nokes, R. I., Lo, H.-Y. & Liu, P. L.-F. 2017 Physical and numerical modelling of tsunami generation by a moving obstacle at the bottom boundary. *Environ. Fluid Mech.* **17**, 929–958.

Zhou, H. & Teng, M. H. 2010 Extended fourth-order depth-integrated model for water waves and currents generated by submarine landslides. *J. Eng. Mech.* **136(4)**, 506–516.

Zhou, Q., Zhan, J. & Li, Y. 2016 High-order finite volume WENO schemes for Boussinesq modelling of nearshore wave processes. *J. Hydraul. Res.* **54**, 646–662.